

Threshold-independent method for single-shot readout of spin qubits in semiconductor quantum dots

Rui-Zi Hu(胡睿梓), Sheng-Kai Zhu(祝圣凯), Xin Zhang(张鑫), Yuan Zhou(周圆), Ming Ni(倪铭), Rong-Long Ma(马荣龙), Gang Luo(罗刚), Zhen-Zhen Kong(孔真真), Gui-Lei Wang(王桂磊), Gang Cao(曹刚), Hai-Ou Li(李海欧), and Guo-Ping Guo(郭国平)

Citation: Chin. Phys. B, 2024, 33 (**1**): 010304. DOI: 10.1088/1674-1056/ace3a9
Journal homepage: http://cpb.iphy.ac.cn; http://iopscience.iop.org/cpb

What follows is a list of articles you may be interested in

Improved quantum (*t*,*n*) threshold group signature

Yaodong Zhang(张耀东), Feng Liu(刘锋), and Haixin Zuo(左海新)
Chin. Phys. B, 2023, 32 (**9**): 090308. DOI: 10.1088/1674-1056/acac0a

Quantum color image scaling based on bilinear interpolation

Chao Gao(高超), Ri-Gui Zhou(周日贵), and Xin Li(李鑫)
Chin. Phys. B, 2023, 32 (**5**): 050303. DOI: 10.1088/1674-1056/ac8f35

Generation of microwave photon perfect *W* states of three coupled superconducting resonators

Xin-Ke Li(李新克), Yuan Zhou(周原), Guang-Hui Wang(王光辉), Dong-Yan Lv(吕东燕),Fazal Badshah, and Hai-Ming Huang(黄海铭)
Chin. Phys. B, 2023, 32 (**4**): 040306. DOI: 10.1088/1674-1056/aca394

High-fidelity universal quantum gates for hybrid systems via the practical photon scattering

Jun-Wen Luo(罗竣文) and Guan-Yu Wang(王冠玉)
Chin. Phys. B, 2023, 32 (**3**): 030303. DOI: 10.1088/1674-1056/ac8734

Realization of the iSWAP-like gate among the superconducting qutrits

Peng Xu(许鹏), Ran Zhang(张然), and Sheng-Mei Zhao(赵生妹)
Chin. Phys. B, 2023, 32 (**2**): 020306. DOI: 10.1088/1674-1056/ac89e7

Threshold-independent method for single-shot readout of spin qubits in semiconductor quantum dots

Rui-Zi Hu(胡睿梓)[1,2], Sheng-Kai Zhu(祝圣凯)[1,2], Xin Zhang(张鑫)[1,2], Yuan Zhou(周圆)[1,2], Ming Ni(倪铭)[1,2], Rong-Long Ma(马荣龙)[1,2], Gang Luo(罗刚)[1,2], Zhen-Zhen Kong(孔真真)[3], Gui-Lei Wang(王桂磊)[3,4], Gang Cao(曹刚)[1,2], Hai-Ou Li(李海欧)[1,2,†], and Guo-Ping Guo(郭国平)[1,2,5]

[1] *CAS Key Laboratory of Quantum Information, University of Science and Technology of China, Hefei* 230026, *China*
[2] *CAS Center For Excellence in Quantum Information and Quantum Physics, University of Science and Technology of China, Hefei* 230026, *China*
[3] *Key Laboratory of Microelectronics Devices and Integrated Technology, Institute of Microelectronics, Chinese Academy of Sciences, Beijing* 100029, *China*
[4] *Beijing Superstring Academy of Memory Technology, Beijing* 100176, *China*
[5] *Origin Quantum Computing Company Limited, Hefei* 230026, *China*

(Received 20 April 2023; revised manuscript received 21 June 2023; accepted manuscript online 3 July 2023)

The single-shot readout data process is essential for the realization of high-fidelity qubits and fault-tolerant quantum algorithms in semiconductor quantum dots. However, the fidelity and visibility of the readout process are sensitive to the choice of the thresholds and limited by the experimental hardware. By demonstrating the linear dependence between the measured spin state probabilities and readout visibilities along with dark counts, we describe an alternative threshold-independent method for the single-shot readout of spin qubits in semiconductor quantum dots. We can obtain the extrapolated spin state probabilities of the prepared probabilities of the excited spin state through the threshold-independent method. We then analyze the corresponding errors of the method, finding that errors of the extrapolated probabilities cannot be neglected with no constraints on the readout time and threshold voltage. Therefore, by limiting the readout time and threshold voltage, we ensure the accuracy of the extrapolated probability. We then prove that the efficiency and robustness of this method are 60 times larger than those of the most commonly used method. Moreover, we discuss the influence of the electron temperature on the effective area with a fixed external magnetic field and provide a preliminary demonstration for a single-shot readout of up to 0.7 K/1.5 T in the future.

Keywords: quantum computation, quantum dot, quantum state readout

PACS: 03.67.Lx, 03.67.–a, 68.65.Hb **DOI:** 10.1088/1674-1056/ace3a9

1. Introduction

Spin qubits in gate-defined silicon quantum dots (QDs) are promising for realizing quantum computation due to their long coherence time,[1,2] small footprint,[3] potential scalability,[4] and industrial manufacturability.[5,6] In isotopically purified Si devices, the single-qubit gate fidelity has attained 99.9%,[7,8] and a two-qubit gate fidelity above 99% has been reported.[9–11] However, the corresponding readout fidelities are lower than 99%, which significantly reduces the overall fidelity of the gate operation. The Elzerman single-shot readout method is usually used,[12,13] which utilizes the spin-state-dependent tunneling rate or quantum capacitance to measure the spin qubits with extra charge sensors or dispersive sensing techniques.[14–16] The spin states are distinguished by comparing the readout traces x with the threshold voltages x_t within the readout time t_r. However, this process is sensitive to x_t and t_r, and will lower the overall fidelity of the gate operations.

Several methods have been developed to optimize the readout fidelity F^R and visibility V^R, as well as to find out the corresponding optimal threshold voltage x_t and readout time t_r, e.g., wavelet edge detection,[17] the analytical expression of the distribution,[18,19] statistical techniques,[21] neural network,[20] digital processing,[22] and the Monte–Carlo method.[23] Among these methods, the Monte–Carlo method is now widely used to numerically simulate the distributions of the experimental data in Si-MOS QDs,[24] Si/SiGe QDs,[25] Ge QDs,[26] single donors,[27] and nitrogen-vacancy centers.[28] A high-fidelity readout in a silicon single spin qubit has recently been achieved.[29] Even so, the readout visibility V^R is limited by the environment and experimental setup, e.g., the external magnetic field relative to the electron temperature (B_{ext}/T_e), relaxation time (T_1), tunneling rate ($\Gamma^{in,out}$), measurement bandwidth, sample rate (Γ_s), and filter frequency.[30]

Here, we describe a threshold-independent method for the single-shot readout of semiconductor spin qubits. By considering the rate equations[30–33] and the Monte–Carlo method, we simulate the single-shot readout process and extract V^R as a function of readout time t_r and threshold voltage x_t. We demonstrate that the measured probability of the excited spin state ($P_\uparrow^M$) is linearly dependent on V^R in Eq. (5). Since the slope is the prepared probability of the excited spin state ($P_\uparrow^I$) and is robust to t_r and x_t, it is convenient to use $P_\uparrow^I$ in-

†Corresponding author. E-mail: haiouli@ustc.edu.cn
© 2024 Chinese Physical Society and IOP Publishing Ltd

stead of $P_{\uparrow}^{\mathrm{M}}$ to realize a threshold-independent data processing method. We then analyzed the error of the fitting process, finding that the error from the bin edges caused a discrepancy between the result and the expected value. We ensured accurate extrapolated probability by choosing readout time t_{r} and threshold voltage x_{t}. Moreover, we use an effective area (A_{eff}) to show the effectiveness of the threshold-independent method, which is approximately 60 times larger than the commonly used method, i.e., the threshold-dependent method. Finally, we discussed the influence of T_{e} on the effective area of both the threshold-independent method and the threshold-dependent method with a fixed external magnetic field, and also provide a preliminary demonstration for a single-shot readout at 0.7 K/1.5 T in the future.

2. Result and discussion

2.1. Single-shot readout

Figure 1 outlines the processes of single-shot readout. The double quantum dots (DQDs) in our experiment resemble the device in Ref. [34]. (N_{L}, N_{R}) in the charge stability diagram in Fig. 1(a) represent the electrons occupied in the left and right QD. To measure the spin state of the first electron in the left QD, we deploy consecutive three-stage pulses, which consist of "empty", "load" & "wait" and "readout" at (0,0)–(1,0) transition line, illustrated by "E", "W" and "R" in black circles in Fig. 1(a). Figure 1(b) shows the corresponding energy states. Here, we assume that the excited spin state is $|\uparrow\rangle$. The location of the readout stage is carefully calibrated to ensure that the Fermi level of the reservoir is between the electrochemical potentials of spin-up and spin-down states.

The readout traces were measured by amplifying the single-electron transistor (SET) current (I_{S}) with a room temperature low noise current amplifier (DLCPA-200) and a JFET preamplifier (SIM910), and then low-pass filtering the amplified signal using an analog filter (SIM965) with a bandwidth of 10 kHz. The blue and red curves represent spin up and spin down traces measured at point R, respectively. We can distinguish the different spin states by comparing the maximum value of each readout trace with the threshold voltage within the readout time.

The state-to-charge (STC) conversion is realized by distinguishing two different traces in the readout phase, as shown in Fig. 1(c). Single electron tunneling onto or off the QD causes a change in the readout trace x. We distinguish the different spin states in the QD by comparing readout trace x with the threshold voltage x_{t}. If x remains below the threshold during the readout phase, we assume it is a $|\downarrow\rangle$ state, and vice versa. We then emptied QDs by raising the electrochemical potential and waited for enough time. After the empty stage, we loaded a new electron with a random spin state and waited for the next readout stage.

We measured the electron spin relaxation time by repeating this three-stage pulse and changing the waiting time in the loading stage. Figure 1(d) shows typical exponential decay of the measured spin-up probability $P_{\uparrow}^{\mathrm{M}} = \rho \cdot \mathrm{e}^{-t/T_1} + \alpha$, where ρ is the amplitude and α is the dark count. Additionally, we can manipulate the spin qubit by using a similar pulse and a microwave pulse, as reported in Ref. [35].

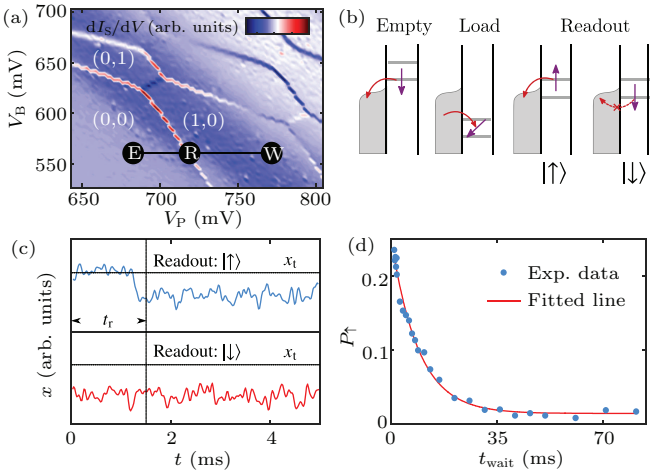


Fig. 1. (a) Charge stability diagram of the DQD measured by differentiating the single-electron transistor (SET) current (I_{S}) as a function of the V_{B} and V_{P} gate voltages. The pulse sequence for measuring the spin relaxation time (T_1) via the (0,0)–(1,0) charge transition line is overlaid on the data. (b) Illustration of the energy states of the pulse sequence: the measurement starts by emptying the electron in the QD at point E, it then injects a random spin into it and waits for a time at point W, and finally moves to point R for STC conversion. (c) The readout traces (x) are achieved by amplifying I_{S} with a room temperature low noise current amplifier (DLCPA-200) and a JFET preamplifier (SIM910), and then low-pass filtering the amplified signal using an analog filter (SIM965) with a bandwidth of 10 kHz. The blue and red curves represent spin up ($|\uparrow\rangle$) and spin down ($|\downarrow\rangle$) traces at point R, respectively. By comparing the maximum of each readout trace (x_{max}) with the threshold voltage (x_{t}) within the readout time (t_{r}), we can distinguish the different spin states. (d) A typical exponential decay of spin-up probability with 1000 repeated measurements for each point. The exponential fit for $1/T_1$ is $112 \pm 6\ \mathrm{s}^{-1}$.

2.2. The readout visibility

We demonstrated a maximum visibility $V^{\mathrm{R}} = 85.4\%$ while measuring the spin relaxation time, as shown in Fig. 2(a). $V^{\mathrm{R}} = F_{\uparrow}^{\mathrm{R}} + F_{\downarrow}^{\mathrm{R}} - 1$ is calculated from the simulated data via the Monte–Carlo method. $F_{\downarrow}^{\mathrm{R}}$ and $F_{\uparrow}^{\mathrm{R}}$ are the readout fidelities of $|\downarrow\rangle$ and $|\uparrow\rangle$. In Fig. 2(b), we simulated the distribution of the single-shot signal with a high accuracy (R squared ≈ 0.98) of the corresponding fitting process (the right-hand inset in Fig 2(b)). The insets in Fig 2(b) show the fitting results of the averaged readout traces ($\bar{x}$) and the probability density function (PDF) of the maximum traces (x_{max}) of the readout phase for every single measurement. The details of the simulation process and the insets in Fig. 2(b) are discussed in Section 1 of the supplementary materials.[23,27,30–32] By fitting $\bar{x}$ with the rate equations, we obtained the tunneling rates of the STC conversion as shown in the left-hand inset of Fig. 2(b): $\Gamma_{\uparrow}^{\mathrm{out}} = 6.0 \pm 0.1$ kHz, $\Gamma_{\downarrow}^{\mathrm{out}} = 27 \pm 2$ Hz and $\Gamma_{\downarrow}^{\mathrm{in}} = 1.39 \pm 0.04$ kHz.

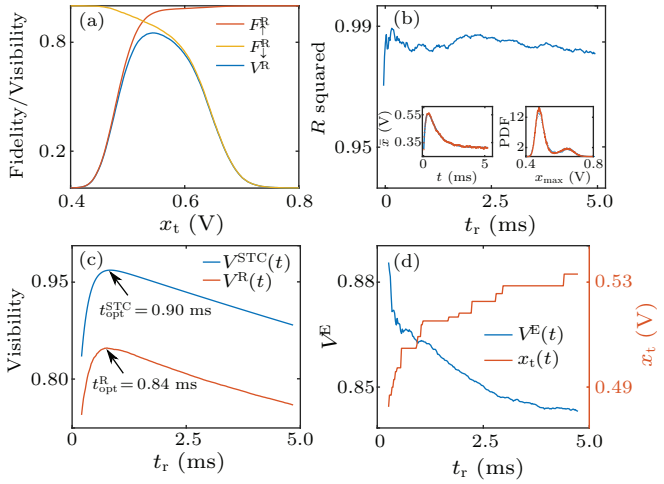


Fig. 2. (a) The fidelities of spin-up and spin-down state ($F_\uparrow^R$,$F_\downarrow^R$) and the related readout visibility (V^R) versus x_t. (b) The fitting model for the distribution of the experimental data has a high value of R squared (≈ 0.98), which indicates the good accuracy of the results. The insets show fitting results for the averaged traces ($\bar{x}$) and the probability density function (PDF) of the maximum value of each readout trace (x_{max}). (c) The state-to-charge (STC) conversion visibility (V^{STC}) versus t_r and the corresponding maximum value V^R. t_{opt}^R (the bottom arrow) and t_{opt}^{STC} (the top arrow) are not equal. (d) The electrical detection visibility (V^E) and the corresponding optimal threshold voltage x_t as a function of readout time t_r.

In the traditional methods, STC conversion visibility (V^{STC}) and electrical detection visibility (V^E) need to be optimized to obtain a high readout visibility V^R. Instead, the threshold-independent single-shot readout method does not need to perform such a cumbersome operation. Here, we introduce the steps of this novel method. First, we calculated V^{STC} as a single peaked function of readout time t_r with the knowledge of tunneling rates as shown in Fig. 2(c). The details of this part are described in Section 2 of the supplementary materials. For exceeding 99% V^{STC}, the following three criteria are given in Ref. [30]: $E_z/T_e > 13$, $T_1 \cdot \Gamma_\uparrow^{out} > 100$ and $\Gamma_s/\Gamma_\downarrow^{in} > 12$. Here, we have $\Gamma_s = 50$ kHz, $B_{ext} = 1.5$ T and $T_e = 180.5 \pm 8.1$ mK, as mentioned in Ref. [34]; thus, the disagreement of the condition $E_z/T_e = 11.22 < 13$ limits the maximum V^{STC} to 97.15%. Figure 2(c) also shows the readout visibility V^R as a single peaked function of t_r (details are discussed in Section 4 of the supplementary materials). However, the optimal readout time t_{opt} for V^{STC} is different from that for V^R. Thus,to obtain the maximum V^R, we should consider the readout time t_r and threshold voltage x_t together.

Due to the lack of a simple analytical expression for the distribution of x_{max}, V^E cannot be obtained directly. Here, we obtain V^E by factorizing V^R into $V^{STC} = F_\uparrow^{STC} + F_\downarrow^{STC} - 1$ and $V^E = F_\uparrow^E + F_\downarrow^E - 1$, as the following formula shows:

$$V^R = F_\uparrow^R + F_\downarrow^R - 1 = V^{STC} \times V^E. \tag{1}$$

Here, readout fidelities $F_\downarrow^R$ and $F_\uparrow^R$ are given by

$$F_\downarrow^R = F_\downarrow^{STC} F_\downarrow^E + (1 - F_\downarrow^{STC})(1 - F_\uparrow^E),$$

$$F_\uparrow^R = F_\uparrow^{STC} F_\uparrow^E + (1 - F_\uparrow^{STC})(1 - F_\downarrow^E), \tag{2}$$

the corresponding readout visibility V^R is obtained from the Monte–Carlo method and the STC visibility V^{STC} is calculated as above. Thus, we have the electrical detection visibility $V^E = V^R/V^{STC}$ indirectly. Figure 2(d) shows the maximum V^E and the corresponding optimal threshold voltage x_t versus readout time t_r. Considering the increasing or constant nature of the maximum value x_t as t_r increases in each readout trace, it can be inferred that the optimal threshold voltage x_t follows a monotonically non-decreasing pattern. Meanwhile, the longer t_r we consider, the more noise is added to the trace. Therefore, it is obvious that V^E will decrease as t_r increases.

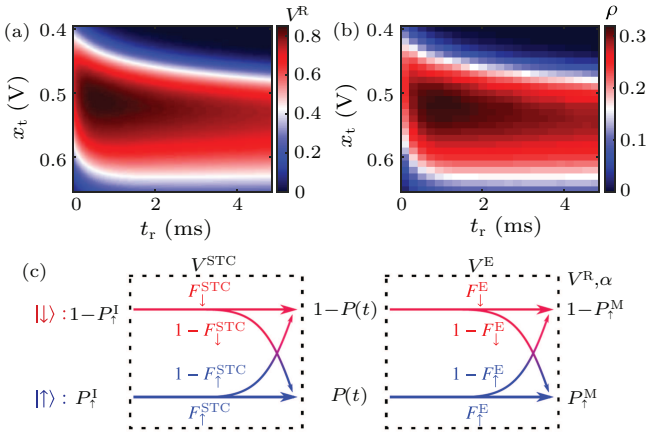


Fig. 3. (a) and (b) The V^R and the amplitude (ρ) as a function of t_r and x_t, showing the consistency in the scaled color image. (c) The qubits are prepared in $|\uparrow\rangle$ with probability $P_\uparrow^I$. Throughout the STC conversion ($F_\uparrow^{STC}$, $F_\downarrow^{STC}$), the electron tunnels out from QD with probability $P(t)$. Similarly, the electrons are measured as $|\uparrow\rangle$ with $P_\uparrow^M$ throughout the electrical detection process($F_\uparrow^E$, $F_\downarrow^E$).

2.3. Relation between $P_\uparrow^M$, $P_\uparrow^I$ and V^R

We now focus on the details of readout visibility V^R. First, we illustrate the relationship between V^R and readout time t_r along with threshold voltage x_t via the Monte–Carlo method in Fig. 3(a). As mentioned in Subsection 2.2, x_t corresponding to the maximum electrical detection visibility V^E increases as t_r increases. The STC visibility V^{STC} is a uni-modal function of t_r. Therefore, V^R increases first and then decreases along the t_r axis, and x_t of the maximum V^R increases along the x_t axis as t_r increases.

We then drew the spin-up probability ρ in the same range in Fig. 3(b) for comparison. The expression $\rho = P_\uparrow^M|_{t_{wait}\to 0} - \alpha$ is obtained by fitting the experimental data of the spin relaxation process with an exponential function $P_\uparrow^M = \rho \cdot e^{-t/T_1} + \alpha$. Here, $\alpha = P_\uparrow^M|_{t_{wait}\to+\infty}$ is the dark count of the spin relaxation process. Figures 3(a) and 3(b) show that the readout visibility V^R and probability ρ are consistent in the scaled color images.

To analyze this consistency, we focus on the details of Eq. (1). As shown in Fig. 3(c), we note the spin-up probability

at the beginning of the readout phase as the prepared probability $P_{\uparrow}^{\mathrm{I}}$. Throughout the STC conversion, the probability of the tunneling events detected within readout time t_{r} ($P(t)$) depends on the condition probability that electrons in $|\uparrow\rangle$ ($F_{\uparrow}^{\mathrm{STC}}$) or $|\downarrow\rangle$ ($1-F_{\downarrow}^{\mathrm{STC}}$) tunnel out:

$$P(t) = F_{\uparrow}^{\mathrm{STC}} P_{\uparrow}^{\mathrm{I}} + (1-F_{\downarrow}^{\mathrm{STC}})(1-P_{\uparrow}^{\mathrm{I}}). \tag{3}$$

Similarly, by comparing the maximum of each readout traces $x_{\max}$ with threshold voltage x_{t}, the electron is measured with $P_{\uparrow}^{\mathrm{M}}$ throughout the electrical detection ($F_{\uparrow}^{E}$, $F_{\downarrow}^{E}$):

$$P_{\uparrow}^{\mathrm{M}} = P(t)F_{\uparrow}^{\mathrm{E}} + (1-P(t))(1-F_{\downarrow}^{\mathrm{E}}). \tag{4}$$

We factorized Eq. (4) into sectors with and without $P_{\uparrow}^{\mathrm{I}}$ and substituted Eq. (2) into Eq. (4) to obtain the expression $\alpha = 1-F_{\downarrow}^{\mathrm{R}}$. The relation between the measured probability $P_{\uparrow}^{\mathrm{M}}$, prepared probability $P_{\uparrow}^{\mathrm{I}}$, and readout visibility V^{R} can then be extracted by substituting Eq. (1) into Eq. (4)

$$P_{\uparrow}^{\mathrm{M}} = P_{\uparrow}^{\mathrm{I}} \times V^{\mathrm{R}} + \alpha. \tag{5}$$

The details of derivation are discussed in Section 6 of the supplementary materials.

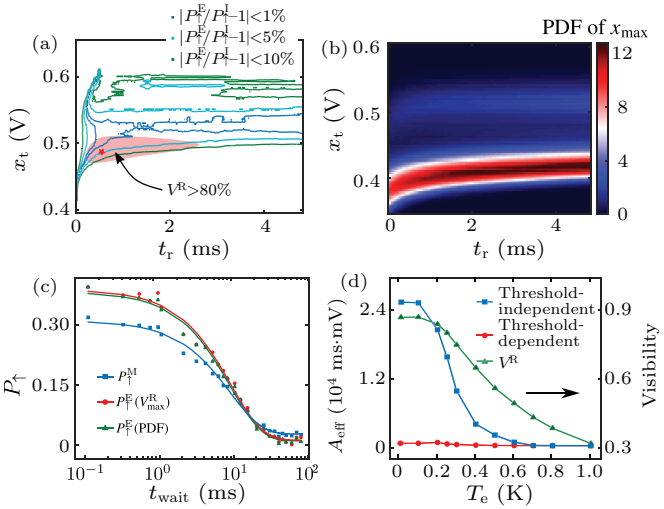


Fig. 4. (a) The bias of the expected probability ($P_{\uparrow}^{\mathrm{E}}$) relative to $P_{\uparrow}^{\mathrm{I}}$ ($P_{\uparrow}^{\mathrm{E}}/P_{\uparrow}^{\mathrm{I}}-1$) as a function of readout time t_{r} and threshold voltage x_{t}. The regions between the blue, cyan, and green curves represent A_{eff} where $|P_{\uparrow}^{\mathrm{E}}/P_{\uparrow}^{\mathrm{I}}-1| < 1\%$, 5% and 10%, respectively. For comparison, the red star represents the position of the maximum readout visibility $V_{\max}^{\mathrm{R}}$, and the points in the pink shadow region satisfy $V^{\mathrm{R}} > 80\%$. (b) The map of the PDF of $x_{\max}$ (maximum of the readout trace). The monotonically non-decreasing feature of the maximum function causes the positions of the two peaks to increase as t_{r} increases. The outline of the valley between two peaks is similar to that of (a). (c) The extrapolated probability $P_{\uparrow}^{\mathrm{E}}$ figured out from the threshold-independent methods at $V_{\max}^{\mathrm{R}}$ (red circles) and minimum between two peaks in PDF of $x_{\max}$ (green triangles). The measured probabilities $P_{\uparrow}^{\mathrm{M}}$ (blue rectangles) are obtained from the exponential decay process at $V_{\max}^{\mathrm{R}}$ directly. The solid curves with the same color illustrate the corresponding exponential fitting results. t_{wait} is logarithmic,showing that the threshold-independent method suppresses dark count α and improves probability ρ. (d) The left-hand y-axis shows that A_{eff} is a function of the electron temperature T_{e} in both threshold-independent method and threshold-dependent readout. The right-hand y-axis shows the corresponding readout visibility V^{R}. When T_{e} exceeds 100 mK, V^{R} and A_{eff} of the threshold-independent methods will decrease as T_{e} increases. The A_{eff} of the threshold-independent method is higher than that of the threshold-dependent method until $T_{\mathrm{e}} = 0.7$ K as V^{R} fixed at 0.5.

Equation (5) reveals that the measured probability $P_{\uparrow}^{\mathrm{M}}$ linearly depends on the readout visibility V^{R} and dark count α. Here, the slope is the prepared probability $P_{\uparrow}^{\mathrm{I}}$ and the intercept is the dark count. By substituting Eq. (5) into the definition of the probability $\rho = P_{\uparrow}^{\mathrm{M}}|_{t_{\mathrm{wait}}\to 0} - \alpha$, we got $\rho = P_{\uparrow}^{\mathrm{I}}|_{t_{\mathrm{wait}}\to 0} \times V^{\mathrm{R}}$. Since $P_{\uparrow}^{\mathrm{I}}$ only depends on the "wait" process, the probability ρ is proportional to the readout visibility V^{R} in the readout process, and this proportional relation between ρ and V^{R} explains their consistency in the scaled color images shown in Figs. 3(a) and 3(b). Since $P_{\uparrow}^{\mathrm{I}}$ only depends on the "wait" process, we try to apply the threshold-independent data process methods in Subsection 2.4.

2.4. Threshold-independent data process

We calculate the extrapolated probability ($P_{\uparrow}^{\mathrm{E}}$) for each t_{r} and x_{t} by applying Eq. (5) directly

$$P_{\uparrow}^{\mathrm{E}} = (P_{\uparrow}^{\mathrm{M}} - \alpha)/V^{\mathrm{R}}. \tag{6}$$

Here, $P_{\uparrow}^{\mathrm{E}}$ is the extrapolated probability and can be calculated from by V^{R} and α. Since $P_{\uparrow}^{\mathrm{I}}$ is independent of the threshold voltage x_{t} and readout time t_{r}, we speculated that the extrapolated probability $P_{\uparrow}^{\mathrm{E}}$ is also threshold independent with no constraints on x_{t} and t_{r}. We calculate the contour map of $|P_{\uparrow}^{\mathrm{E}}/P_{\uparrow}^{\mathrm{I}}-1|$, as shown in Fig. 4(a). The region inside the blue, cyan, and green curves represent the area where $|P_{\uparrow}^{\mathrm{E}}/P_{\uparrow}^{\mathrm{I}}-1| < 1\%$, 5% and 10%, respectively. We compared the regions with the visibility V^{R} map in Fig. 4(a). The pink shadow represents where $V^{\mathrm{R}} > 80\%$, and the red star represents the position of $V_{\max}^{\mathrm{R}}$. There is a discrepancy between $|P_{\uparrow}^{\mathrm{E}}/P_{\uparrow}^{\mathrm{I}}-1|$ and the V^{R} map, revealing that the optimal x_{t} and t_{r} for the readout visibility V^{R} are not optimal for $P_{\uparrow}^{\mathrm{E}}$.

In Section 5 of the supplementary materials, we will use the simulated traces to illustrate that the region $|P_{\uparrow}^{\mathrm{E}}/P_{\uparrow}^{\mathrm{I}}-1| < 1\%$ almost covers the whole considered region under ideal circumstances. We calculated the cumulative error (CE) and absolute value of error between the distribution of experimental and simulated traces as a function of threshold voltage x_{t}. The shape of the CE curve demonstrates that the error in the fitting process comes from the bin edges. The features of the bin edge error are shown in the contour map of $|P_{\uparrow}^{\mathrm{E}}/P_{\uparrow}^{\mathrm{I}}-1|$ in Figs. 22(b) and 22(c) in the supplementary materials.

In the valley region between the two peaks, errors from bin edges are minimal, as shown in the map of the distribution of $x_{\max}$ in Fig. 4(a). The outline of the valley region in Fig. 4(b) resembles that of $|P_{\uparrow}^{\mathrm{E}}/P_{\uparrow}^{\mathrm{I}}-1| < 1\%$ and 5% in Fig. 4(a). As a compromise method, we can choose x_{t} around the minimum between two peaks of the distribution of $x_{\max}$ instead of x_{t} at $V_{\max}^{\mathrm{R}}$.

By using the threshold-independent method to processing the experimental data, we calculated the extrapolated probability $P_{\uparrow}^{\mathrm{E}}$ t_{r} and threshold voltage x_{t} at $V_{\max}^{\mathrm{R}}$ ($P_{\uparrow}^{\mathrm{E}}(V_{\max}^{\mathrm{R}})$), along

with the minimum between two peaks in PDF of the maximum of each readout trace $x_{\max}$ with the same $t_{\rm r}$ ($P_{\uparrow}^{\rm E}$(PDF)). Figure 4(c) shows $P_{\uparrow}^{\rm E}$ as a function of waiting time of the spin decaying process $t_{\rm wait}$, and we plot measured probability $P_{\uparrow}^{\rm M}$ for comparison. The results demonstrate that the threshold-independent method suppresses dark count α and increases probability $\rho = P_{\uparrow}^{\rm M}|_{t_{\rm wait}\to 0} - \alpha$, and $P_{\uparrow}^{\rm E}$(PDF) calculated via the compromise method is slightly different from $P_{\uparrow}^{\rm E}(V_{\max}^{\rm R})$. $x_{\rm t}$ and readout time $t_{\rm r}$ in a wider range with only a 1% loss of accuracy.

Finally, we tried to use the area where $|P_{\uparrow}^{\rm E}/P_{\uparrow}^{\rm I} - 1| < 1\%$ as $A_{\rm eff}$ to quantify the accuracy and efficiency of different data processing methods. For comparison, we use the area of where $|P_{\uparrow}^{\rm M}/P_{\uparrow}^{\rm I} - 1| < 1\%$ as $A_{\rm eff}$ for the commonly used threshold-dependent method. The $A_{\rm eff}$ of the threshold-independent method is 60 times larger than that of the threshold-dependent method, meaning that we can choose threshold voltage $x_{\rm t}$ and readout time $t_{\rm r}$ in a 60 times larger range and maintain 99% accuracy. In addition, the threshold-independent method is more robust and can calibrate the measured result from the interference of the experimental hardware limitation.

2.5. Influence of the electron temperature

We try to characterize the influence of $T_{\rm e}$. Reference [30] assumes that the tunneling rate follows a Fermi distribution

$$\begin{aligned} \Gamma_{\uparrow,\downarrow}^{\rm out} &= [1 - f(\varepsilon \pm E_z/2,\ T_{\rm e})]\Gamma^{\rm out}, \\ \Gamma_{\uparrow,\downarrow}^{\rm in} &= f(\varepsilon \pm E_z/2,\ T_{\rm e})\Gamma^{\rm in}, \end{aligned} \tag{7}$$

where $f(\varepsilon \pm E_z/2,\ T_{\rm e})$ is the Fermi–Dirac function with $-$ for $|\downarrow\rangle$ and $+$ for $|\uparrow\rangle$, $\Gamma^{\rm out}$ ($\Gamma^{\rm in}$) is the maximum tunnel out (in) rate, $\Gamma_{\uparrow,\downarrow}^{\rm out}$ ($\Gamma_{\uparrow,\downarrow}^{\rm in}$) are tunneling rates of corresponding spin state, and ε is the energy splitting between the Fermi energy of the electron reservoir and the average energy of $|\uparrow\rangle$ and $|\downarrow\rangle$ electrons in QD. Therefore, $\varepsilon + E_z/2$ ($\varepsilon - E_z/2$) represents the energy splitting between the Fermi energy of the electron reservoir and the energy state of $|\uparrow\rangle$ ($|\downarrow\rangle$) electron in QD.

By defining $R_G = \Gamma_{\uparrow}^{\rm out}/\Gamma_{\downarrow}^{\rm out}$, ε can be obtained as follows:

$$\varepsilon = -k_{\rm B}T_{\rm e}\ln\left(\frac{1-R_{\rm G}}{R_{\rm G}}\frac{1}{{\rm e}^{\frac{-E_z}{2k_{\rm B}T_{\rm e}}} - {\rm e}^{\frac{E_z}{2k_{\rm B}T_{\rm e}}}}\right). \tag{8}$$

We extracted the maximum tunneling rates $\Gamma^{\rm out}$ and $\Gamma^{\rm in}$ by substituting ε into Eq. (7).

We then tried to simulate the single-shot readout process at different electron temperatures $T_{\rm e}$. Assuming that tunneling rates $\Gamma^{\rm out}$ and $\Gamma^{\rm in}$ are not associated with $T_{\rm e}$, we directly substituted $T_{\rm e}$ into Eq. (7) to calculate the tunneling rates. We used the Monte–Carlo method to generate the simulated traces with a fixed external magnetic field $B_{\rm ext} = 1.5$ T at different $T_{\rm e}$. The left-hand y-axis in Fig. 4(d) shows the $A_{\rm eff}$ of both the threshold-independent method and the threshold-dependent method at different $T_{\rm e}$. The right-hand y-axis shows the corresponding readout visibility $V^{\rm R}$. The simulation results show that the $A_{\rm eff}$ of the threshold-independent methods is 60 times greater than that of the threshold-dependent method when $T_{\rm e} < 0.1$ K. As $T_{\rm e}$ increases, $A_{\rm eff}$ of the threshold-independent methods decreases. It is larger than that of the threshold-dependent method until $T_{\rm e} = 0.7$ K. When $T_{\rm e} > 0.7$ K, the corresponding $V^{\rm R} < 0.5$. Here, we can give the boundary condition of the threshold-independent method as $T_{\rm e} = 0.7$ K when $B_{\rm ext} = 1.5$ T.

3. Summary

We described a threshold-independent method of the single-shot readout data process based on the linear dependence of measured probability $P_{\uparrow}^{\rm M}$ with the corresponding readout visibility $V^{\rm R}$ and dark count α. Due to the error during the fitting process from bin edges, the extrapolated probability deviates from the prepared probability. For compromise, the region of readout time $t_{\rm r}$ and threshold voltage $x_{\rm t}$ are reduced to the minimum of the distribution of the maximum of each readout trace $x_{\max}$ to ensure that the accuracy loss of extrapolated probability $P_{\uparrow}^{\rm E}$ is less than 1%. We then used $A_{\rm eff}$ to quantify the efficiency of the threshold-independent method and the threshold-dependent readout. The result shows that the $A_{\rm eff}$ of the threshold-independent method is more than 60 times larger than that of the threshold-dependent method. Moreover, we simulated the single-shot readout process at different electron temperatures $T_{\rm e}$. We broaden the boundary condition of the single-shot readout to 0.7 K with $B_{\rm ext} = 1.5$ T, where $V^{\rm R} = 0.5$. The significance of employing the threshold-independent method will progressively increase as the experiment advances towards the fault-tolerance threshold of the logic qubit, particularly when operating under high electron temperature conditions.[36–38]

Acknowledgements

Project supported by the National Natural Science Foundation of China (Grant Nos. 12074368, 92165207, 12034018, and 62004185), the Anhui Province Natural Science Foundation (Grant No. 2108085J03), the USTC Tang Scholarship, and this work was partially carried out at the USTC Center for Micro and Nanoscale Research and Fabrication.

References

[1] Muhonen J T, Dehollain J P, Laucht A, *et al*. 2014 *Nat. Nanotech.* **9** 986
[2] Zhang X, Li H O, Cao G, *et al*. 2019 *National Science Review* **6** 32
[3] Dodson J P, Holman N, Thorgrimsson B, *et al*. 2020 *Nanotechnology* **31** 505001
[4] Li R, Petit L, Franke D P, *et al*. 2018 *Science Advances* **4** eaar3960

[5] Camenzind L C, Geyer S, Fuhrer A, *et al.* 2022 *Nat. Electron.* **5** 178
[6] Zwerver A M J, Krähenmann T, Watson T F, *et al*. 2022 *Nat. Electron.* **5** 184
[7] Yoneda J, Takeda K, Otsuka T, *et al*. 2018 *Nat. Nanotech.* **13** 102
[8] Chan K W, Huang W, Yang C H, *et al*. 2018 *Phys. Rev. Applied* **10** 044017
[9] Xue X, Russ M, Samkharadze N, *et al*. 2022 *Nature* **601** 343
[10] Noiri A, Takeda K, Nakajima T, *et al*. 2022 *Nature* **601** 338
[11] Mills A R, Guinn C R, Gullans M J, *et al.* 2022 *Science Advances* **8** eabn5130
[12] Elzerman J, Hanson R, van Beveren L W, *et al*. 2004 *Nature* **430** 431
[13] Zajac D, Hazard T, Mi X, Nielsen E and Petta J R 2016 *Phys. Rev. Applied* **6** 054013
[14] Pakkiam P, Timofeev A V, House M G, *et al*. 2018 *Phys. Rev. X* **8** 041032
[15] West A, Hensen B, Jouan A, *et al*. 2019 *Nat. Nanotech.* **14** 437
[16] Zheng G, Samkharadze N, Noordam M L, *et al*. 2019 *Nat. Nanotech.* **14** 742
[17] Prance J R, Bael B J V, Simmons C B, *et al*. 2015 *Nanotechnology* **26** 215201
[18] Nowack K C, Shafiei M, Laforest M, *et al*. 2011 *Science* **333** 1269
[19] D'Anjou B and Coish W A 2014 *Phys. Rev. A* **89** 012313
[20] Gorman S K, He Y, House M G, *et al*. 2017 *Phys. Rev. Applied* **8** 034019
[21] Struck T, Lindner J, Hollmann A, Schauer F, Schmidbauer A, Bougeard D and Schreiber L R 2021 *Scientific Reports* **11** 16203
[22] Mizokuchi R, Tadokoro M and Kodera T 2020 *Appl. Phys. Express* **13** 121004
[23] Morello A, Pla J J, Zwanenburg F A, *et al*. 2010 *Nature* **467** 687
[24] Veldhorst M, Hwang J C C, Yang C H, *et al*. 2014 *Nat. Nanotech.* **9** 981
[25] Kawakami E, Scarlino P, Ward D R, *et al*. 2014 *Nat. Nanotech.* **9** 666
[26] Vukušić L, Kukučka J, Watzinger H, *et al*. 2018 *Nano Lett.* **18** 7141
[27] Büch H, Mahapatra S, Rahman R, *et al*. 2013 *Nat. Commun.* **4** 2017
[28] Robledo L, Childress L, Bernien H, *et al*. 2011 *Nature* **477** 574
[29] Adam R Mills, *et al.* 2022 *Science Advances* **8** eabn5130
[30] Keith D, Gorman S, Kranz L, *et al*. 2019 *New J. Phys.* **21** 063011
[31] Xiao M, House M and Jiang H W 2010 *Phys. Rev. Lett.* **104** 096801
[32] Tracy L A, Lu T M, Bishop N C, *et al*. 2013 *Appl. Phys. Lett.* **103** 143115
[33] House M G, Xiao M, Guo G, *et al*. 2013 *Phys. Rev. Lett.* **111** 126803
[34] Zhang X, Hu R Z, Li H O, *et al*. 2020 *Phys. Rev. Lett.* **124** 257701
[35] Hu R Z, Ma R L, Ni M, *et al*. 2021 *Nanomaterials* **11** 2486
[36] Huang W, Yang C H, Chan K W, *et al*. 2019 *Nature* **569** 532
[37] Petit L, Eenink H G J, Russ M, *et al*. 2020 *Nature* **580** 355
[38] Takeda K, Noiri A, Nakajima T, *et al*. 2021 *Nat. Nanotech.* **16** 965